Journal of Solid State Chemistry 183 (2010) 65–75

Contents lists available at ScienceDirect

Journal of Solid State Chemistry

journal homepage: www.elsevier.com/locate/jssc

# $Sn_x[BPO_4]_{1-x}$ composites as negative electrodes for lithium ion cells: Comparison with amorphous $SnB_{0.6}P_{0.4}O_{2.9}$ and effect of composition

Donato Ercole Conte [a,*], Abdelmaula Aboulaich [a], Florent Robert [a,1], Josette Olivier-Fourcade [a], Jean-Claude Jumas [a], Christian Jordy [b], Patrick Willmann [c]

[a] Institut Charles Gerhardt—Equipe Agrégats, Interfaces et Matériaux pour l'Energie, UMR 5253-CNRS, Université Montpellier II, Place E. Bataillon, 34095 Montpellier, France
[b] SAFT, 111-113 Bd. A. Daney, 33074 Bordeaux Cedex, France
[c] CNES, Centre Spatial de Toulouse, 18 Avenue Edouard Belin, 31401 Toulouse, France

ARTICLE INFO

*Article history:*
Received 9 September 2009
Received in revised form
16 October 2009
Accepted 22 October 2009
Available online 29 October 2009

*Keywords:*
Sn-based composites
Lithium-ion batteries
Negative electrodes
Mössbauer spectroscopy
$Li_xSn$ alloys

ABSTRACT

A comparative study of two Sn-based composite materials as negative electrode for Li-ion accumulators is presented. The former $SnB_{0.6}P_{0.4}O_{2.9}$ obtained by *in-situ* dispersion of SnO in an oxide matrix is shown to be an amorphous tin composite oxide (ATCO). The latter $Sn_{0.72}[BPO_4]_{0.28}$ obtained by *ex-situ* dispersion of Sn in a borophosphate matrix consists of Sn particles embedded in a crystalline $BPO_4$ matrix. The electrochemical responses of ATCO and $Sn_{0.72}[BPO_4]_{0.28}$ composite in galvanostatic mode show reversible capacities of about 450 and 530 mAh $g^{-1}$, respectively, with different irreversible capacities (60% and 29%). Analysis of these composite materials by $^{119}$Sn Mössbauer spectroscopy in transmission (TMS) and emission (CEMS) modes confirms that ATCO is an amorphous $Sn^{II}$ composite oxide and shows that in the case of $Sn_{0.72}[BPO_4]_{0.28}$, the surface of the tin clusters is mainly formed by $Sn^{II}$ in an amorphous interface whereas the bulk of the clusters is mainly formed by $Sn^0$. The determination of the recoilless free fractions $f$ (Lamb–Mössbauer factors) leads to the effective fraction of both $Sn^0$ and $Sn^{II}$ species in such composites. The influence of chemical composition and especially of the surface-to-bulk tin species ratio on the electrochemical behaviour has been analysed for several $Sn_x[BPO_4]_{1-x}$ composite materials ($0.17 < x < 0.91$). The cell using the compound $Sn_{0.72}[BPO_4]_{0.28}$ as active material exhibits interesting electrochemical performances (reversible capacity of 500 mAh $g^{-1}$ at C/5 rate).



## 1. Introduction

Lithium ion batteries have become considerable interest in various fields of applications ranging from electronic devices, to electric and hybrid vehicles or space applications.

Since the first Li-ion battery commercialized by Sony, using $Li_xC_6$ as negative electrode, an intensive research has been undertaken to search for new negative materials with the aim to increase their energy density.

Many metallic anode materials, pure metals or alloys, have been studied showing higher capacities than graphite (372 mAh $g^{-1}$). Among them, metallic Sn is known to have one of the highest theoretical capacities when used as a lithium storage electrode, with a value of 991 mAh $g^{-1}$ corresponding to a fully lithiated composition of $Li_{4.4}Sn$. However, the use of tin or its alloys in rechargeable cells has been hindered by drastic volume changes occurring during lithium alloying–dealloying reactions, which cause cracking of the electrode material and finally loss of electrical contact between the single particles. As a consequence the capacity fades rapidly. To overcome this disadvantage, several methods have been proposed. One consists in the use of superfine materials, such as $Sn/SnSb_x$, $Sn/SnAg_x$ (200–400 nm) [1,2], nano-Sn (~10 nm) [3,4] and nano-SnSb (20–100 nm) [5]. Intermetallic compounds have been widely investigated, for example $Cu_6Sn_5$ [6,7], $CoSn_2$ [8] and Mg–Sn [9,10]. A feature article recently published summarizes the state-of-the-art in the field of pure metal as negative materials [11].

The announcement of the *Stalion* battery by Fuji Photo Film Co. [12] using a new class of anode material based on an amorphous tin composite oxide (ATCO) of the form $SnM_xO_y$ (where $M$ is a group III or V glass forming element such as $B^{III}$, $P^V$ and $Al^{III}$) has stimulated intense discussion on the use of Sn-based composites as negative electrode for lithium ion batteries [13–15]. In such amorphous materials, showing a high reversible capacity (~600 mAh $g^{-1}$), the $Sn^{II}$ atoms are dispersed into an oxide glass, typically a borophosphate amorphous material. For the composi-

* Corresponding author. Fax: +33 4 67 14 33 04.
*E-mail address:* iguanasornione@libero.it (D.E. Conte).
[1] Present address: Laboratoire Matériaux et molécules en milieu amazonien (L3MA/UMR ECOFOG/IESG), 2091 Route de Baduel—BP 792, 9337 Cayenne.

0022-4596/$ - see front matter © 2009 Elsevier Inc. All rights reserved.
doi:10.1016/j.jssc.2009.10.015

tion $Sn^{II}B_{0.6}P_{0.4}O_{2.9}$ the lithium insertion mechanism has been studied in detail by means of X-ray diffraction (XRD), X-ray absorption (XAS), *in situ* and *ex situ* $^{119}$Sn transmission Mössbauer spectroscopy (TMS) [16,17]. This study revealed a complex reduction mechanism in two steps. During the first step the main reaction corresponds to a $Sn^{II} \rightarrow Sn^0$ reduction leading to the *in-situ* formation of a Sn/amorphous oxide composite. The second step corresponds to a Li–Sn alloying process with the formation of Li–Sn bonds. The reversible part of this second step can be explained from the formation of small particles of Li–Sn alloys in interaction with the oxygen atoms in the glass matrix. Although the vitreous support presents an interesting dispersal effect, the main drawback of these ATCO materials is the large irreversible capacity in the first discharge (400 mAh $g^{-1}$) due to the reduction of $Sn^{II}$ to $Sn^0$.

More recently *ex-situ* Sn particles dispersion into an electrochemically inactive matrix has been proposed as new strategy [18]. This procedure leads to composite materials like Sn/$BPO_4$ or Sn/$CaSiO_3$ in which Sn particles are embedded in a crystallized $BPO_4$ or $CaSiO_3$ matrixes. During the synthesis of such composites via a ceramic route, Sn and oxide particles react to form an interface between them that improves the cohesion of the composite. In the case of Sn:$BPO_4$ composite, as evidenced by $^{119}$Sn conversion electron Mössbauer spectroscopy (CEMS) which is sensitive to tin atoms within layer of few hundreds of nm, this interface has been identified as a $Sn^{II}$ amorphous borophosphate [19,20]. Such composites show a high reversible capacity (550 mAh $g^{-1}$) close to that obtained for the best ATCO materials (600 mAh $g^{-1}$) and a lower irreversible capacity of 200 mAh $g^{-1}$. The same concept of *in-situ* formation of active atoms dispersed in inert phases is used for materials with lower irreversible charge losses, the best results so far having been obtained with a composite of active $SnFe_2$ and inactive $SnFe_3C$ [21,22].

In the first part of the present work, we report a comparative study between ATCO and a new Sn/$BPO_4$ composite material obtained by *ex-situ* dispersion of Sn into an electrochemically inactive $BPO_4$ matrix. The recoilless free fractions *f* (Lamb–Mössbauer factors) of the different tin species have been evaluated from $^{119}$Sn TMS spectra recorded at different temperatures, in order to determine the effective fractions of each species.

In the second part, the influence of the Sn/$BPO_4$ ratio on the electrochemical performances of the electrode material has been studied.

## 2. Experimental section

### 2.1. Synthesis

The $Sn_{0.72}[BPO_4]_{0.28}$ composite was prepared by a two-steps solid state reaction method. In a first step, $BPO_4$ was synthesized from equimolar amounts of $NH_4H_2PO_4$ (Acros Organics) and $H_3BO_3$ (Acros Organics) as phosphoric and boric precursors. The starting materials were ground in an agate mortar and placed in an alumina crucible. De-ionized water was added in order to form a homogeneous white paste that was heated in a furnace to 380 °C for about 13 h.

In the second step, $BPO_4$ was mixed with Sn powder (Aldrich) in the desired molar ratio. This mixture was heated in a vitreous carbon vessel inside a horizontal tube furnace to 500 °C for 7 h in a constant flow of nitrogen and was then quenched to room temperature by removing the vessel from the furnace. Final grinding gives a grey powder.

The tin oxide composite glass $SnB_{0.6}P_{0.4}O_{2.9}$ is prepared by a solid-state reaction. A stoichiometric mixture of SnO (synthesized in the laboratory [23]), of $NH_4H_2PO_4$ (as the $P_2O_5$ precursor) and of $B_2O_3$ (Aldrich) was heated in a vitreous carbon boat inside a horizontal tube furnace. The sample was first heated to 180 °C for 15 h so as to avoid the quick decomposition of $NH_4H_2PO_4$ into $P_2O_5$, $NH_3$ and $H_2O$, then heated to 800 °C for 15 h in a constant flow of argon, and finally quenched to room temperature by removing the boat from the furnace. The glass formed was almost clear and gave off a white powder after grinding.

### 2.2. Characterization

The stoichiometry of the samples was checked by inductively coupled plasma atomic emission spectroscopy (ICP-AES) in the laboratories of CNRS (Centre National de Recherche Scientifique) in Solaize (Fr).

The powdered samples were analysed by X-ray diffraction (XRD) on a PHILIPS X'Pert MPD equipped with an X'celerator detector. The pattern was recorded in the $\theta$–$2\theta$ continuous mode using Cu$K\alpha$ radiation ($\lambda$=1.5418 Å) in order to determine the structural properties of the different samples.

Electrochemical tests were carried out on electrodes containing 90 wt% sample and 10 wt% carbon black (Y50A) electronic conductor as cathode material and lithium metal as anode. Standard Swagelok$^{TM}$ cells Li | 1M $LiPF_6$ in propylene carbonate (PC):ethylene carbonate (EC):dimethyl carbonate (DMC) 1:1:3 | ATCO or $Sn_{0.72}[BPO_4]_{0.28}$ composite were assembled in an argon-filled glove box. The cells were tested using a Mac-Pile® system in the galvanostatic mode with two potential windows of 0.1–1 and 0.01–1.2 V versus $Li^+/Li^0$ at C/5 rate (C/*n* expressed as 1 mole of $Li^+$ reacted in *n* hours). The $Sn_x[BPO_4]_{1-x}$ ($0.17 < x < 0.91$) composites were tested at C rate instead. We chose a faster rate both for practical reasons and to test the composites behaviour under highly stressing conditions.

$^{119}$Sn TMS spectra were recorded in the constant acceleration mode using components manufactured by ORTEC and WISSEL. Low temperature spectra were recorded in a flow cryostat from Air Liquide using liquid nitrogen or helium as cooling agent. A $Ca^{119m}SnO_3$ source with a nominal activity of 370 MBq was used which was kept at room temperature in all experiments. $^{119}$Sn CEMS spectra were recorded on the same spectrometer using a gas flow (94% He, 6% methane) proportional counter to detect the internal conversion electrons emitted after resonant absorption of gamma rays. All CEMS data were recorded at room temperature. The velocity scale was calibrated with the magnetically split sextet spectrum of a high-purity α-Fe foil as the reference absorber, using a $^{57}$Co (Rh) source. The spectra were fitted to Lorentzian profiles by the least-squares method using the ISOfit program [24]. The goodness of fits was controlled by a classical $\chi^2$ test. All isomer shifts are given with respect to the room temperature spectrum of $BaSnO_3$. The maximum experimental error on hyperfine parameters is estimated to $\pm$0.05 mm/s. In the case of $Sn_x[BPO_4]_{1-x}$, two components were used to fit all the spectra. One sub-spectrum gives small quadrupole splitting (QS) and isomer shift (IS) corresponding to metallic tin. The second sub-spectrum gives large QS and IS similar to those observed for $Sn^{II}$ species [20,25,26] and attributed here to the amorphous part observed with XRD. We chose not to fix the values of hyperfine parameters corresponding to β-Sn ($\delta$=2.56 mm/s, $\Delta$=0.29 mm/s [27,28], see Fig. 3). Instead we preferred to first evaluate the line width at half-maximum of the $Sn^{II}$ sub-spectrum and then to fix it for the overall treatment of the recorded spectra (this is represented as "*" in Tables 3 and 6). This is not valid for the tin poor $Sn_x[BPO_4]_{1-x}$ compositions ($x$=0.17 and 0.25) where the too small amount of metallic tin required it to be fixed at the β-Sn parameters (see Table 6). A similar effect is encountered when the β-Sn is lightly detected within CEMS spectra.

### 2.3. Determination of the effective fractions of Sn species in the obtained composites

The recoilless fraction (or Lamb–Mössbauer factor) "*f*", represents the probability of a nuclear transition (absorption or emission) without variation of the vibrational state of the lattice spectrum. Its value depends on the rigidity of the tin-containing lattice at a given temperature. This can be deduced from the relation

$$f = \exp[-k^2 \langle x^2 \rangle] \quad (1)$$

where $k$ is the wave vector of the γ-ray and $<x^2>$ is the mean square of vibrational amplitude in the direction of the γ-ray, averaged over all amplitudes in the half lifetime of the excited nuclear state. Assuming a Debye model for the solid, one has considered the large number of oscillator levels and their distribution. Each of these levels has a certain probability of being excited by the recoil. Quantitatively from the Debye model, the following expression for the recoil-free fraction can be deduced:

$$f \cong \exp\left[\frac{-3E_\gamma^2 T}{k_B M c^2 \theta_D^2}\right] \quad (2)$$

where $k_B$ is the Boltzmann constant, $E_\gamma$ is the γ-ray energy for the selected isotope, $T$ is the absolute temperature, $\theta_D$ the Debye temperature of the lattice and $M$ is the mass of the absorbing atom. Herber suggests [29] to replace the Debye temperature $\theta_D$ by the lattice temperature $\theta_M$ measured by Mössbauer spectroscopy. For a thin absorber the temperature dependence of the $f$ factor is well represented by the temperature dependence of the area $A$ under the resonance curve. Thus, the following equation can be used to determine $\theta_M$:

$$\frac{d(\ln A_{(T)})}{dT} = \frac{-3E_\gamma^2}{k_B M c^2 \theta_M^2} \quad (3)$$

where $A_{(T)}$ is the spectral area of the phase under consideration and $M$ is the mass of the free Mössbauer atom.

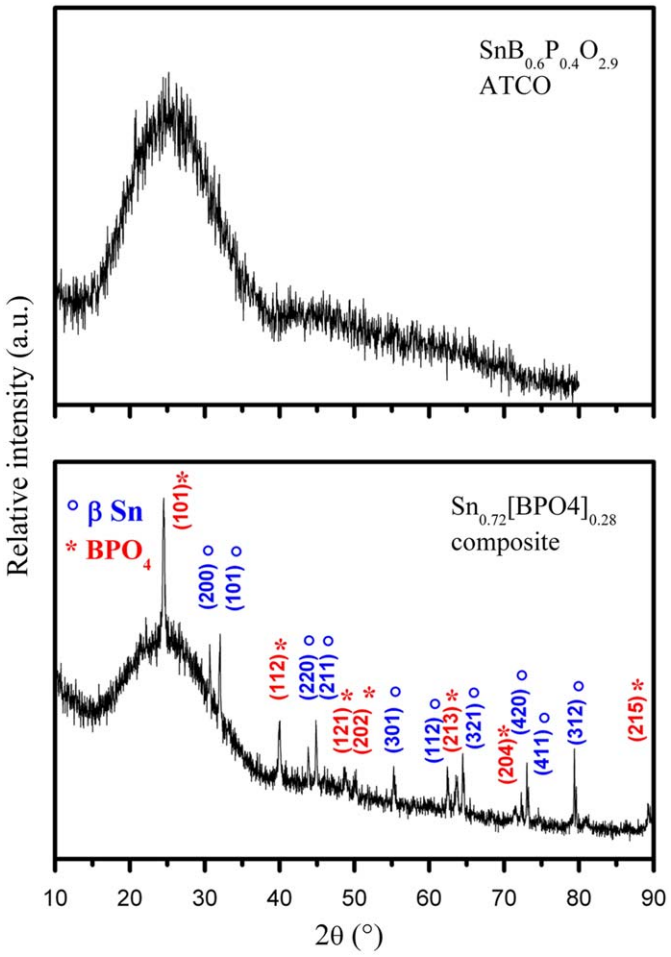


**Fig. 1.** X-ray diffraction patterns of ATCO ($SnB_{0.6}P_{0.4}O_{2.9}$) and $Sn_{0.72}[BPO_4]_{0.28}$ composite materials ($\lambda_{CuK\alpha}$=1.5418 Å).

## 3. Results and discussion

The XRD patterns of both the $SnB_{0.6}P_{0.4}O_{2.9}$ ATCO and the $Sn_{0.72}[BPO_4]_{0.28}$ composite material are shown in Fig. 1.

As expected, the XRD data of $SnB_{0.6}P_{0.4}O_{2.9}$ show the absence of long-range order in the pristine glass sample that confirms its amorphous structure. The diffraction lines observed for the $Sn_{0.72}[BPO_4]_{0.28}$ composite are those of pure β-Sn and $BPO_4$ and have been indexed according to two tetragonal units. The cell parameters have been determined from a least-squares fit using an appropriate computer program [30]. The obtained values are in agreement with previously published data: $a$=5.820 Å, $c$=3.175 Å for β-Sn [31] and $a$=4.332 Å, $c$=6.640 Å for $BPO_4$ [32,33]. We note also the presence of a broad diffusion domain in the 20–34 $2\theta^\circ$ range which has been attributed to an amorphous component in the composite.

The electrochemical response of ATCO glass and $Sn_{0.72}[BPO_4]_{0.28}$ composite in galvanostatic mode at C/5 rate is shown in Fig. 2.

For ATCO, the discharge capacity (lithiation process) in first cycle was 1107 mAh $g^{-1}$ or 7.1 equivalent mole of Li ion per mole of material, from which 451 mAh $g^{-1}$ (3.1 equivalent Li ion per mole of material) could be returned upon charge at 1 V. This represents 60% of capacity loss during the first electrochemical charge. The behaviour of this compound thus, does not vary so much if a narrower potential window is used. If we compare with Idota et al. [13], there is a difference of only 100 mAh $g^{-1}$ in the initial cycle due to our slightly slower cycling rate. For the $Sn_{0.72}[BPO_4]_{0.28}$ composite, 799 mAh $g^{-1}$ (4.8 equivalent mole of Li per mole of material) were consumed in first lithiation and 530 mAh $g^{-1}$ (3.4 equivalent Li per mole of material) were recovered during the de-lithiation process, which correspond only to 29% of irreversible capacity. In the case of ATCO, the *in-situ* formation of active elements during the first electrochemical cycle (with the formation of inactive $Li_2O$ from $Sn^{II}$–O active species) contributes to the large irreversible capacity. This process is minimized in the $Sn_{0.72}[BPO_4]_{0.28}$ composite which exhibits better electrochemical performances (lower irreversible capacity and higher reversible capacity) even with the presence of oxidized tin ($Sn^{II}$, see Fig. 3 and Table 5).

A deeper insight in the local environment of tin atoms in both materials can be obtained by $^{119}$Sn Mössbauer spectroscopy. Fig. 3 shows both the experimental data and the fitted curves of the TMS spectrum recorded at room temperature for ATCO (Fig. 3a), CEMS (Fig. 3b) and TMS spectra (Fig. 3c) for $Sn_{0.72}[BPO_4]_{0.28}$ composite.

The spectrum obtained for ATCO presents an asymmetry in line intensity and line width. Consequently, it has been fitted by using two components (Fig. 3a), labelled $Sn_{(1)}^{II}$ and $Sn_{(2)}^{II}$ in Tables 1, 2, 4, 5. The values of isomer shift (IS) and quadrupole splitting (QS) obtained for the two tin species are similar to those described in the literature for $Sn^{II}$ silicate glasses [34], $Sn^{II}$ borates glasses [35] or amorphous $Sn^{II}$ oxides [36].

Two components are also observed for the $Sn_{0.72}[BPO_4]_{0.28}$ composite both in the TMS and CEMS spectra. One sub-spectrum is fitted with small QS and IS corresponding to $Sn^0$. Anyway the Mossbauer probe results in a deeper insight in evaluating the nature of this metallic tin. Where the XRD data show the presence

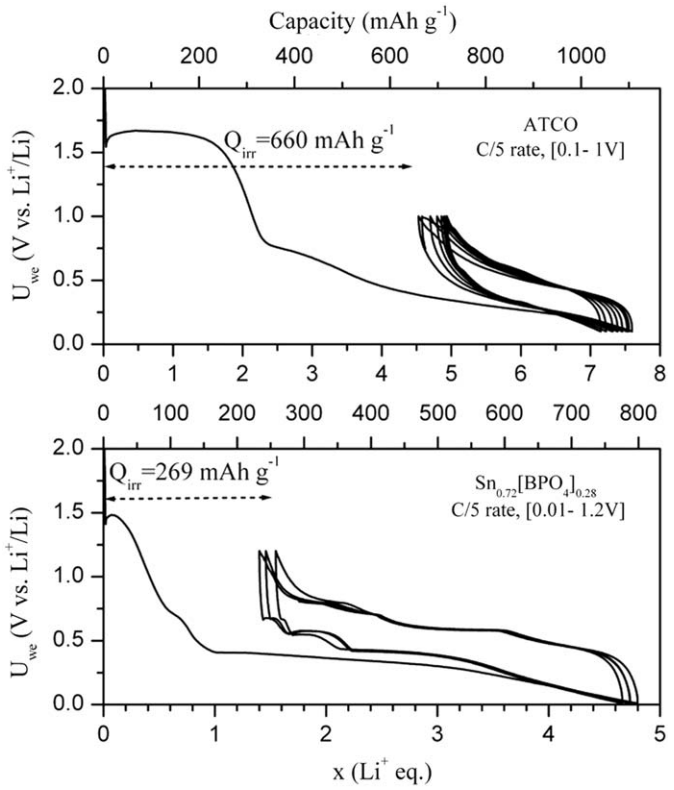


**Fig. 2.** Galvanostatic discharge–charge curves of ATCO and $Sn_{0.72}[BPO_4]_{0.28}$ composite materials at C/5 rate.

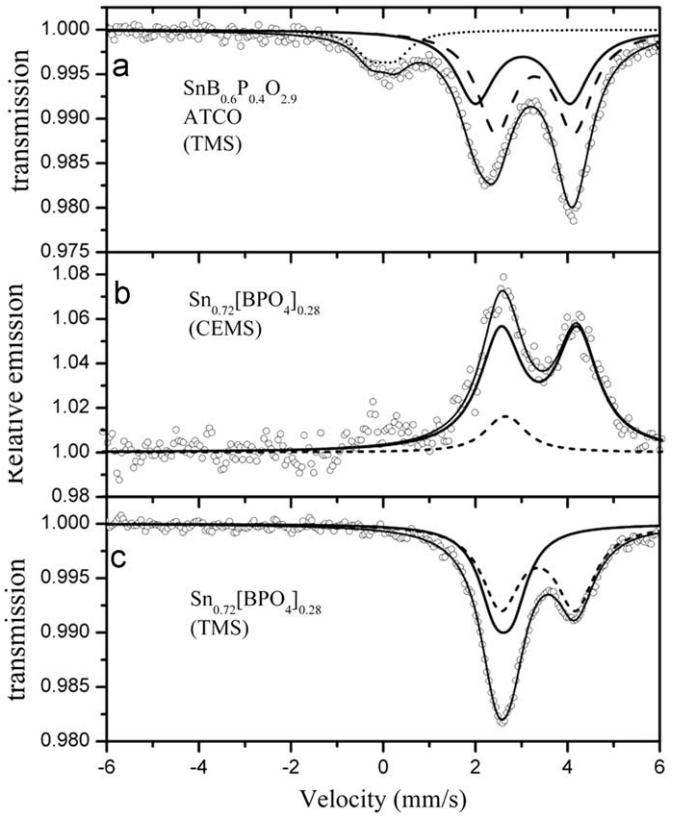


**Fig. 3.** $^{119}$Sn Mössbauer spectra recorded in (a) TMS mode for ATCO, (b) CEMS mode and (c) TMS mode for $Sn_{0.72}[BPO_4]_{0.28}$ composite, respectively, at room temperature. Open circles denote the experimental data and the calculated spectrum is denoted by solid bold line. The different contributions to the spectra are denoted by a dotted line for β-Sn, a dashed line for $Sn^{II}$ and short dotted line for $Sn^{IV}$ (accidental $SnO_2$).

of β-Sn, we cannot fit the spectra according to exact β-Sn specie (Tables 1 and 4). The second sub-spectrum with large QS and IS, is similar to those observed for $Sn_{(2)}^{II}$ in ATCO. Experimental data were treated firstly by two non-constrained singlets in order to evaluate the line width at half-maximum belonging to the $Sn^{II}$ specie. The obtained value was then imposed in the final treatment leaving untouched all the other parameters. It is worth to note however, that this kind of treatment is not always easy to use. Spectra where the $Sn^0$ quantity is too small (small asymmetry of the recorded data) cannot be fitted according to the above procedure. We imposed then the values for the β-Sn specie [27,28] keeping in mind that what we have in the composite is close but not exactly β-Sn. Concerning the $Sn^{II}$ sub-spectrum, we already evidenced the similarity with $Sn_{(2)}^{II}$ in ATCO. In this case, the $Sn^{II}$ specie is responsible for the partial amorphisation observed for the $Sn_{0.72}[BPO_4]_{0.28}$ composite (Fig. 1) as TMS and XRD data agree.

Table 1 summarizes the Mössbauer parameters and the structural differences between ATCO and $Sn_{0.72}[BPO_4]_{0.28}$ composite material.

A first glance on the relative fractions of the different phases, show that the peak area of $Sn^0$ is more important in the bulk material (TMS) than in the close to surface region. In contrast to the conventional transmission geometry, which probes the bulk material, Mößbauer spectroscopy in scattering geometry (CEMS) is sensitive to the "near surface" layers. The de-excitation deriving from the excited nuclear state in the absorber (after resonant absorption of a photon from the source) takes place via one of the following three channels: (i) re-emission of a γ-photon, (ii) absorption of this photon by an electron from an inner shell, which is then ejected, (iii) filling of the core hole remaining after (ii) by electron transitions from higher levels with emission of characteristic X-ray lines. In this study, we have been able to detect the conversion electrons generated from process (ii). One has to keep in mind that CEMS calculated emission depth for bulky β-Sn is between 200 and 400 nm [37]. It is then possible to locate the $Sn^{II}$ specie at the interface between $Sn^0$ grains and $BPO_4$ as we proposed recently [19,38].

**Table 1**
Summary of the Mössbauer parameters and the structural differences between ATCO and $Sn_{0.72}[BPO_4]_{0.28}$ composite studied by XRD and $^{119}$Sn Mössbauer spectroscopy.

| Characterization | $SnB_{0.6}P_{0.4}O_{2.9}$ ATCO | $Sn_{0.72}[BPO_4]_{0.28}$ composite |
|---|---|---|
| X-ray diffraction | Amorphous | β-Sn, $BPO_4$ and amorphous part |
| $^{119}$Sn Mössbauer spectroscopy | | |
| Bulk (TMS) | $Sn^{II}$<br>(1) IS=3.02(3) mm/s<br>QS=2.06(5) mm/s<br>(2) IS=3.29(3) mm/s<br>QS=1.70(4) mm/s | $Sn^0$ (essentially)<br>IS=2.51(2) mm/s<br>QS=0.39(3) mm/s |
| Surface (CEMS) | | $Sn^{II}$ (essentially)<br>IS=3.27(2) mm/s<br>QS=1.62(3) mm/s |

However, these peak areas reflect only the spectral weight of the various species. It must be kept in mind that, at a given temperature, only a fraction $f_{(T)}$ of the $^{119}$Sn nuclei absorbs the γ-rays without recoil and contributes to the Mössbauer spectrum. This $f$ factor, as said in the experimental section, depends on the

**Table 2**
Hyperfine parameters obtained from $^{119}$Sn Mössbauer spectra recorded at different temperatures for the $SnB_{0.6}P_{0.4}O_{2.9}$ ATCO glass.

| Temperature (K) | Site | $\delta$ | $\Delta$ | $\Gamma$ | SF | $\chi^2$ |
|---|---|---|---|---|---|---|
| 88 | $Sn^{II}$ (1) | 3.10 (1) | 1.94 (1) | 1.01 (3) | 55 (1) | 1.03 |
| | $Sn^{II}$ (2) | 3.50 (1) | 1.78 (1) | 0.90 (3) | 33 (1) | |
| 100 | $Sn^{II}$ (1) | 3.08 (1) | 1.93 (1) | 1.04 (4) | 60 (1) | 1.26 |
| | $Sn^{II}$ (2) | 3.49 (1) | 1.81 (1) | 0.93 (4) | 34 (1) | |
| 115 | $Sn^{II}$ (1) | 3.07 (1) | 1.93 (1) | 0.97 (3) | 61 (2) | 1.29 |
| | $Sn^{II}$ (2) | 3.48 (1) | 1.79 (1) | 0.93 (4) | 38 (2) | |
| 130 | $Sn^{II}$ (1) | 3.07 (1) | 1.95 (2) | 0.97 (3) | 58 (3) | 1.32 |
| | $Sn^{II}$ (2) | 3.44 (1) | 1.78 (3) | 0.91 (3) | 41 (2) | |
| 160 | $Sn^{II}$ (1) | 3.06 (1) | 1.96 (2) | 0.96 (5) | 52 (3) | 1.99 |
| | $Sn^{II}$ (2) | 3.40 (1) | 1.76 (3) | 0.90 (4) | 44 (2) | |
| 200 | $Sn^{II}$ (1) | 3.05 (3) | 1.98 (2) | 0.95 (5) | 47 (3) | 1.61 |
| | $Sn^{II}$ (2) | 3.36 (2) | 1.75 (3) | 0.94 (4) | 47 (3) | |
| 240 | $Sn^{II}$ (1) | 3.04 (2) | 1.99 (3) | 0.94 (4) | 45 (4) | 1.36 |
| | $Sn^{II}$ (2) | 3.35 (3) | 1.74 (3) | 0.91 (4) | 48 (3) | |
| 296 | $Sn^{II}$ (1) | 3.02 (3) | 2.06 (5) | 0.96 (3) | 39 (4) | 1.25 |
| | $Sn^{II}$ (2) | 3.29 (3) | 1.70 (4) | 0.95 (4) | 51 (3) | |

Isomer shifts relative to $BaSnO_3$ $\delta$ (mm/s), quadruple splitting $\Delta$ (mm/s), line width at half-maximum $\Gamma$ (mm/s), relative area of the sub-spectra SF (%) and $\chi^2$.

rigidity of the tin-containing lattice at a given temperature. The more rigid the lattice is (i.e. the stronger the bonds Sn is involved in are), the higher will be the recoilless fraction. Thus, the peak area of each species must be corrected for the corresponding $f$ factor, when a quantitative analysis is to be carried out.

As the $f$ factors of the two tin sites in ATCO have not yet been reported in the literature, we undertook their determination from a series of Mössbauer spectra in the temperature range 88–295 K. Fig. 4 and Table 2 show the experimental spectra and the values of the hyperfine parameters, respectively.

The presence of tin in the oxidation state IV ($Sn^{IV}$) with an isomer shift close to 0 mm/s is due to an accidental oxidation of tin leading to the formation of $SnO_2$. In the literature, two values are reported for $f(SnO_2)$ at room temperature (295 K): 0.56 [39] and 0.47 [40]. Due to this high value, the relative amount of $SnO_2$ is overestimated at room temperature and decreases gradually with temperature. Its contribution has been estimated of about 3%.

In Fig. 5 and Table 3 the experimental spectra and the values of the hyperfine parameters for the composite $Sn_{0.72}[BPO_4]_{0.28}$ are reported. The determination of the $f$ factor has been undertaken in the temperature range 77–293 K.

Fig. 6(a and b) shows the variation of the logarithm of the normalized peak area $Ln(A_{(T)}/A_{(5\,K)})$ for $Sn_{(1)}^{II}$ and $Sn_{(2)}^{II}$ with temperature for ATCO.

A linear decrease is found between 100 and 296 K with different slopes for the two tin species

$$\text{For } Sn^{II}\ (1): \frac{d\text{Ln}[A_1(T\text{K})/A(100\text{K})]}{dT} = -6.62\times10^{-3}\,\text{K}^{-1}$$

$$\text{For } Sn^{II}\ (2): \frac{d\text{Ln}[A_2(T\text{K})/A(100\text{K})]}{dT} = -3.69\times10^{-3}\,\text{K}^{-1}$$

The $\theta_M$ values are deduced from Eq. (3)

$\theta_M(Sn_1) = 220(5)$ K and $\theta_M(Sn_2) = 164(5)$ K

The existence of two different values of lattice temperature (220 K for $Sn_{(1)}^{II}$ and 164 K for $Sn_{(2)}^{II}$) confirms the different nature of the two Sn species in the glass lattice (glass modifier and former, respectively). Finally, using Eq. (2) we can calculate the $f$ factors for each $Sn^{II}$ species at a given temperature. The results are given in Table 4.

At room temperature, the $f$ factor of $Sn_{(1)}^{II}$ (0.14) is lower than that of $Sn_{(2)}^{II}$ (0.33). The relative amount of $Sn_{(1)}^{II}$ is thus largely underestimated (Table 5). It is therefore necessary to correct the spectral fractions (SF) (*cfr*. Fig. 3) for the different $f$ factors in order to obtain the effective fractions (EF) of the two species $Sn_{(1)}^{II}$ and $Sn_{(2)}^{II}$, using the following equation:

$$EF_i = \frac{SF_i/f_i}{\sum_i SF_i/f_i} \quad (4)$$

In conclusion, the ATCO materials contains a large proportion of $Sn_{(1)}^{II}$ (61%) that indicates the great participation of $Sn^{II}$ as a network former in tin borophosphate glass (Table 5), whereas, the $Sn_{(2)}^{II}$ can be ascribable to network modifier in the glass.

In order to elucidate the interaction between the initial β-Sn and the $BPO_4$ matrix we evaluated, with the same technique described above, the $f$ factor for the Sn powder (Aldrich, 99.9%). This is also helpful since a wide range of values can be found in the literature [41]. A value of $f_{(300\,K)}$ β-Sn=0.050(2) has been obtained for this commercial product (Table 4).

For the $Sn_{0.72}[BPO_4]_{0.28}$ composite, Fig. 6(c and d) shows the variation of the logarithm of the normalized peak area $Ln(A_{(T)}/A_{(77\,K)})$ for $Sn^0$ and $Sn^{II}$ with temperature. A linear decrease is found between 214 and 293 K with different slopes for the two tin species.

$$\text{For } Sn^0: \frac{d\text{Ln}[A_1(T\text{K})/A(214\text{K})]}{dT} = -9.1\times10^{-3}\,\text{K}^{-1}$$

$$\text{For } Sn^{II}: \frac{d\text{Ln}[A_2(T\text{K})/A(214\text{K})]}{dT} = -7\times10^{-3}\,\text{K}^{-1}$$

The $\theta_M$ values are deduced from Eq. (3)

$\theta_M(Sn^0) = 139(5)$ K and $\theta_M(Sn^{II}) = 159(5)$ K

The values of lattice temperature of the two Sn species are different both respect to bulky β-Sn and to glass modifier $Sn^{II}$.

Finally, using Eq. (2) we can calculate the $f$ factors for each species at a given temperature. The results are given in Table 4.

For this material the effective fractions of each species can be calculated by correcting for the individual $f$ factors of each species (*cfr*. Fig. 3), using the same equation to calculate EF (Table 5). In such $Sn_{0.72}[BPO_4]_{0.28}$ composite, 44% of Sn atoms are used to form the interface species which appear to be very similar to the network modifier specie in the ATCO glass. We can explain the existing differences if we take in account the different environments which surround the tin species: $Sn^0$ is not exactly β-Sn due to its partial transformation in interfacial $Sn^{II}$ and to the relatively

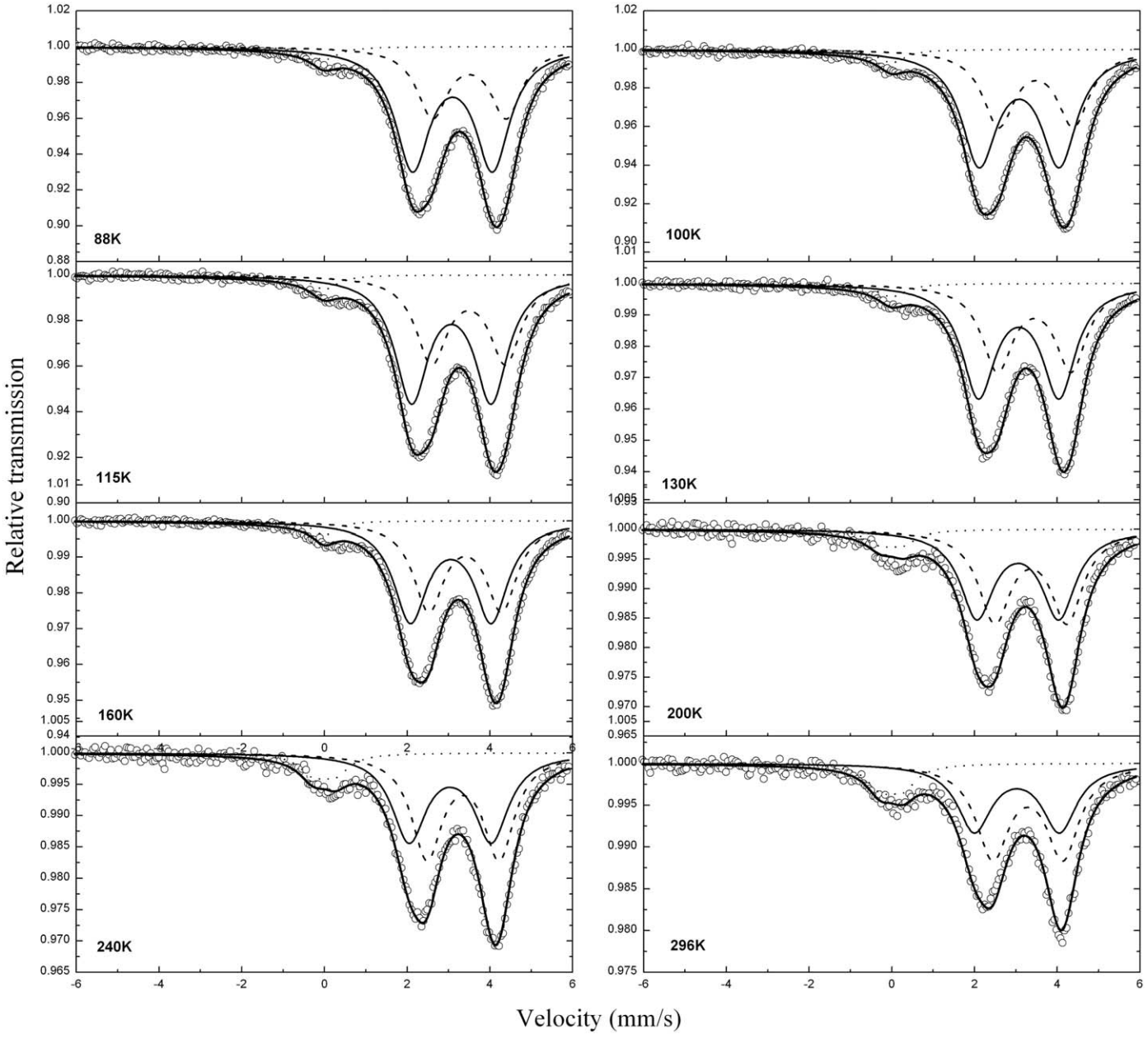


**Fig. 4.** $^{119}$Sn Mössbauer spectra of the $SnB_{0.6}P_{0.4}O_{2.9}$ glass recorded at different temperatures. Open circles denote the experimental data and the calculated spectrum is denoted by solid bold line. The different sub-spectra are denoted by a dashed line for $Sn^{II}$ (site 1 and 2) and a dotted line for $Sn^{IV}$ ($SnO_2$).

small domains. This is also confirmed by the two different values of *f* factor found for the initial β-Sn (Aldrich) and the reacted one. Fig. 7 illustrates this effect where a variation in the normalized area indicates different lattice rigidity for the two species.

On the other hand, $Sn^{II}$ is different from the specie $Sn_{(2)}^{II}$ found in ATCO because it is not bulky but only surfacially coating the metallic particles in a thin layer.

## 4. Influence of the Sn/$BPO_4$ ratio on the electrochemical performances

The XRD patterns (Fig. 8) of the different $Sn_x[BPO_4]_{1-x}$ compositions show a progressive inversion of the intensities of the borophosphate and Sn lines from $x$=0.17 to 0.91. For the last composition ($x$=0.91), the small quantity of borophosphate matrix and the important amount of dispersed tin do not make it possible to see the amorphous part characteristic of the interface formed between the two species observed for other composition between 20 and 34 $2\theta(^\circ)$.

The Mössbauer spectra recorded at room temperature (Table 6) for the different samples show two main contributions: a first unresolved doublet ($\delta$=2.5–2.6 mm/s) with small quadrupole splitting ($\Delta$=0.3–0.6 mm/s) and a second doublet ($\delta$=3.16–3.30 mm/s) with a large quadrupole splitting ($\Delta$=1.5–1.8 mm/s).

As explained previously, only for the slightly asymmetrical spectra the hyperfine parameters were fixed to the well-known values of the β-phase of metallic tin ($\delta$=2.56 mm/s, $\Delta$=0.29 mm/s [27,28]) according to the XRD data. The values of isomer shift and quadrupole splitting of the second doublet are similar to those of $Sn_{(2)}^{II}$ for ATCO as evidenced in the first part of this paper.

The effective fractions of each species were calculated by correcting for the individual *f* factors of each species, using for $Sn^0$

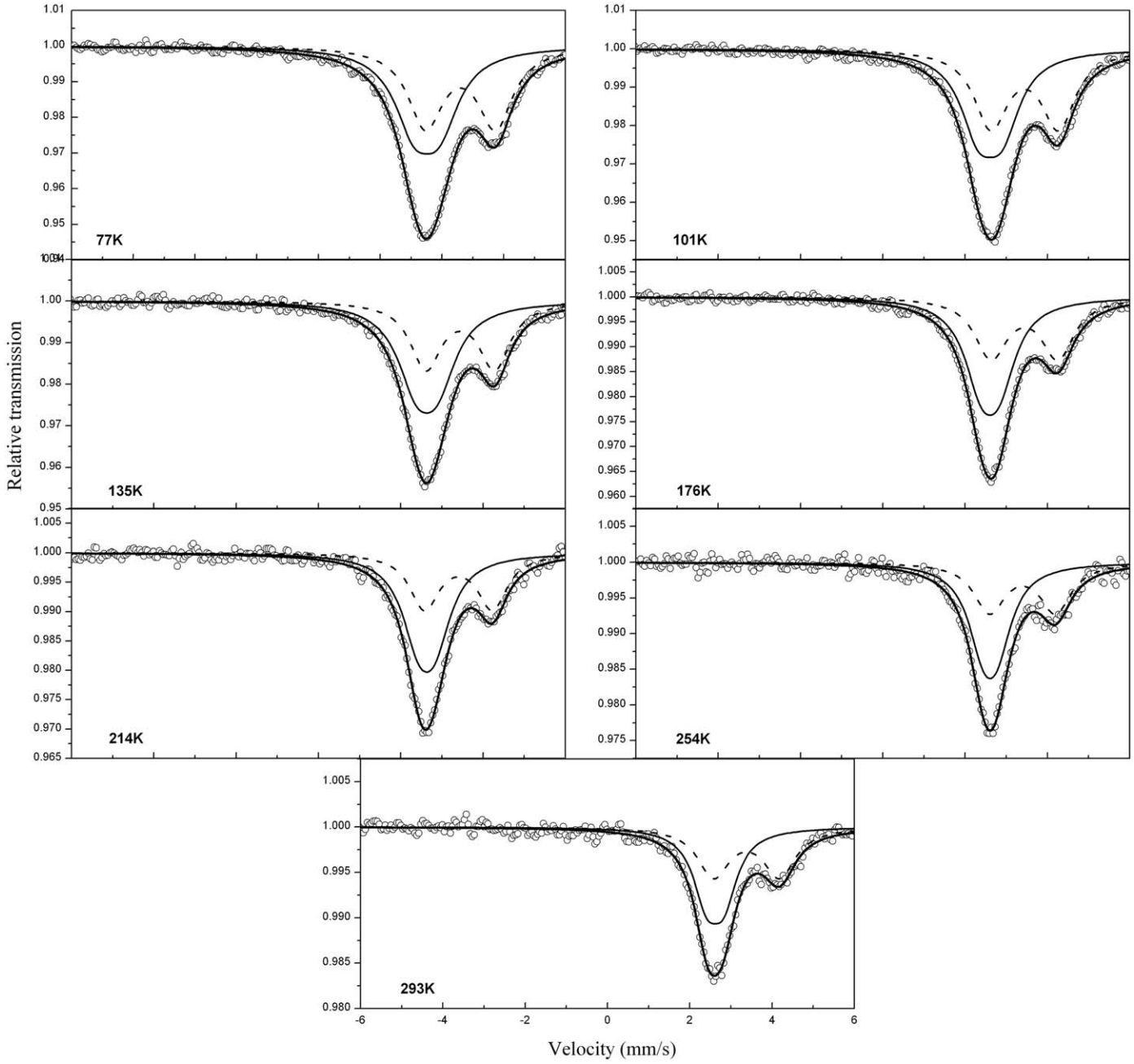


**Fig. 5.** $^{119}$Sn Mössbauer spectra of the $Sn_{0.72}[BPO_4]_{0.28}$ composite recorded at different temperatures. Open circles denote the experimental data and the calculated spectrum is denoted by solid bold line. The different sub-spectra are denoted by a dotted line for $Sn^0$ (essentially β-Sn) and dashed line for $Sn^{II}$.

and $Sn^{II}$ the values previously determined (0.07(1) and 0.12(3)). For each composition, the higher relative contribution of amorphous $Sn^{II}$ borophosphate in the CEMS spectra as compared to the TMS spectra indicates that this $Sn^{II}$ species are situated at the surface of the sample. This is interpreted as a glassy interface formed between $Sn^0$ particles and the $BPO_4$ matrix. The evolutions of effective proportions of β-Sn and interfacial $Sn^{II}$ species on the surface (CEMS) and for the bulk material (TMS) as a function of $Sn/BPO_4$ ratio in the composite are shown in Fig. 9.

For small amounts of dispersed Sn ($x \leq 0.25$), all tin reacts with boron phosphate and forms the amorphous $Sn^{II}$ borophosphate. For $x > 0.25$, the increase of tin leads to the formation of metallic clusters. Consequently, the fraction of $Sn^{II}$ on at the interface decreases whereas that of metallic $Sn^0$ increases in the bulk material (full squares and full triangles in Fig. 9). As regards the near surface parts (hollow squares and hollow triangles in Fig. 9), it is worth to note that this trend is present but averagely slows down when $x \geq 0.5$. For tin richer compositions, we have a sort of stabilization of the $Sn^{II}$ specie measured by CEMS spectroscopy probably indicating that oxidized tin is present along all the analysed thickness. This can explain the similarity of electrochemical behaviour for the compositions $0.5 \leq x \leq 0.72$ as visible in Fig. 10 where the electrochemical behaviour of all compositions was studied in the galvanostatic mode at C rate (1Li/h) in the voltage range 0.01–1.2 V vs. $Li^+/Li$. Above $x=0.72$, we evidently have a too large contribution of $Sn^0$ which goes to detriment of the electrochemical behaviour.

Moreover, the discharge capacities of all cells are lower than the theoretical specific capacity of pure metallic tin (991 mAh $g^{-1}$) and a large irreversible capacity is observed in all cases. The

specific capacity retained is particularly low when the $Sn/BPO_4$ ratio is very high ($x > 0.77$). On the contrary, for lower values of $Sn/BPO_4$ ($x < 0.72$), we shown that the cyclability is relatively better but the specific capacity decreases.

The best electrochemical behaviour is observed for $x = 0.72$ with a relatively high specific capacity and good cycling stability after 10 cycles at C rate. However, this composite material still shows an important irreversible capacity due to

**Table 3**
Hyperfine parameters obtained from $^{119}Sn$ Mössbauer spectra recorded at different temperatures for the $Sn_{0.72}[BPO_4]_{0.28}$ composite.

| Temperature (K) | Site | $\delta$ | $\Delta$ | $\Gamma$ | SF | $\chi^2$ |
|---|---|---|---|---|---|---|
| 77 | $Sn^0$ | 2.54 (1) | 0.62 (2) | 1.20 (3) | 51 (2) | 0.52 |
| | $Sn^{II}$ | 3.36 (1) | 1.70 (1) | 1.00 (*) | 49 (1) | |
| 101 | $Sn^0$ | 2.52 (1) | 0.60 (2) | 1.09 (3) | 51 (2) | 0.45 |
| | $Sn^{II}$ | 3.35 (1) | 1.65 (1) | 0.95 (*) | 49 (1) | |
| 135 | $Sn^0$ | 2.54 (2) | 0.52 (3) | 1.14 (4) | 57 (3) | 0.53 |
| | $Sn^{II}$ | 3.35 (1) | 1.67 (2) | 0.89 (*) | 43 (2) | |
| 176 | $Sn^0$ | 2.52 (1) | 0.45 (2) | 1.01 (3) | 57 (2) | 0.48 |
| | $Sn^{II}$ | 3.35 (1) | 1.63 (2) | 0.92 (*) | 43 (2) | |
| 214 | $Sn^0$ | 2.54 (2) | 0.40 (4) | 0.98 (4) | 59 (4) | 0.50 |
| | $Sn^{II}$ | 3.31 (2) | 1.65 (4) | 0.87 (*) | 41 (4) | |
| 254 | $Sn^0$ | 2.58 (4) | 0.21 (9) | 0.90 (6) | 58 (8) | 0.54 |
| | $Sn^{II}$ | 3.21 (3) | 1.79 (5) | 0.90 (*) | 42 (7) | |
| 293 | $Sn^0$ | 2.52 (2) | 0.42 (3) | 0.82 (4) | 53 (7) | 0.51 |
| | $Sn^{II}$ | 3.29 (3) | 1.60 (5) | 0.90 (*) | 47 (6) | |

Isomer shifts relative to $BaSnO_3$ $\delta$ ($mm\,s^{-1}$), quadruple splitting $\Delta$ ($mm\,s^{-1}$), line width at half-maximum $\Gamma$ ($mm\,s^{-1}$), relative area of the sub-spectra SF (%) and $\chi^2$. "*" represents fixed values.

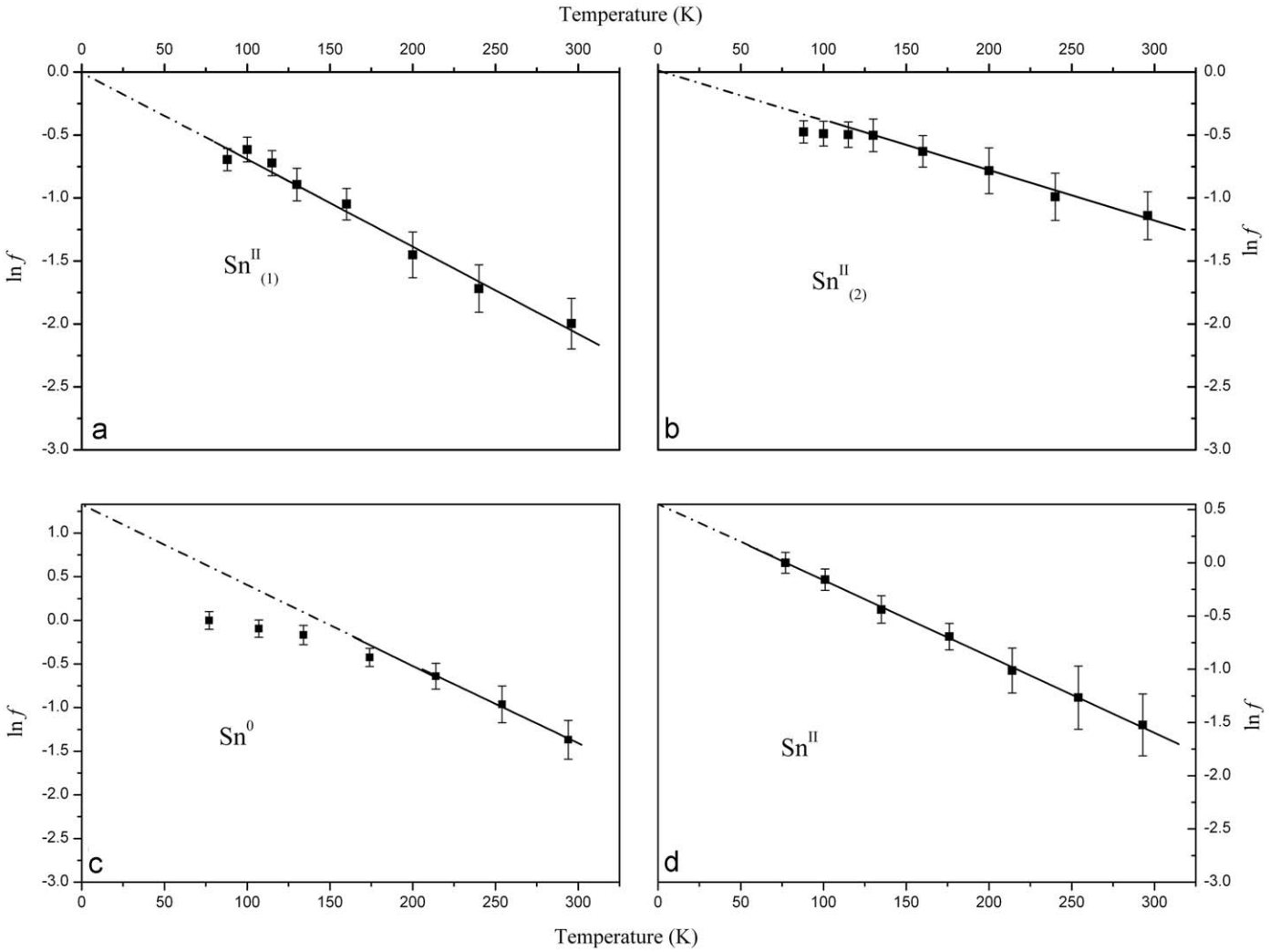


**Fig. 6.** Evolution of logarithm of the normalized peak area for (a) $Sn^{II}_{(1)}$ (b) $Sn_{(2)}{}^{II}$ in the $SnB_{0.6}P_{0.4}O_{2.9}$ ATCO glass and (c) $Sn^0$ (d) $Sn^{II}$ in the $Sn_{0.72}[BPO_4]_{0.28}$ composite.

**Table 4**
Values of Lamb–Mössbauer factors $f$ and lattice temperatures obtained for $Sn^{II}_{(1)}$ and $Sn^{II}_{(2)}$ in $SnB_{0.6}P_{0.4}O_{2.9}$ ATCO glass and for reference compounds (β-Sn, SnO and $SnO_2$).

| $SnB_{0.6}P_{0.4}O_{2.9}$ ATCO | **$Sn^{II}_1$** | $Sn^{II}_2$ | **β-Sn** [33,34] | **SnO** [25] | $SnO_2$ [36] |
|---|---|---|---|---|---|
| $((dLn[A(TK)/A(100\,K)])/dT)$ ($K^{-1}$) | $-6.62\times10^{-3}$ | $-3.69\times10^{-3}$ | | | |
| $f$ (77 K) | 0.59 | 0.74 | 0.35 (1) | 0.74 (1) | 0.76 (1) |
| $f$ **(300 K)** | **0.14 (2)** | 0.33 **(1)** | 0.04 **(1)** | 0.35 **(1)** | **0.56; 0.47** |
| $\theta_M$ (K) | 220 (5) | 164 (5) | 186–195 [ref] | 230 (3) | 243 (3) |
| | | | **β-Sn** (this work) | | |
| $f$ **(300 K)** | | | **0.050 (2)** | | |
| $Sn_{0.72}[BPO_4]_{0.28}$ | **$Sn^{II}$** | | **$Sn^0$** | | |
| $((dLn[A(TK)/A(200\,K)])/dT)$ ($K^{-1}$) | $-7\times10^{-3}$ | | $-9.1\times10^{-3}$ | | |
| $f$ **(300 K)** | 0.12 **(3)** | | 0.07 **(1)** | | |
| $\theta_M$ (K) | 159 (5) | | 139 (5) | | |

**Table 5**
Hyperfine parameters calculated from $^{119}$Sn Mössbauer spectra at 296 K for $SnB_{0.6}P_{0.4}O_{2.9}$ ATCO glass and at 295 K for $Sn_{0.72}[BPO_4]_{0.28}$ relative to Fig. 3 transmission spectra.

| Temperature (K) | Site | $\delta$ (mm/s) | $\Delta$ (mm/s) | $\Gamma$ (mm/s) | SF (%) | $f$ | EF (%) | $\chi^2$ |
|---|---|---|---|---|---|---|---|---|
| 296 | I | 3.02 (2) | 2.06 (3) | 0.96 (3) | 39 (4) | 0.14 (2) | 61 | 0.58 |
| | II | 3.29 (2) | 1.70 (3) | 0.95 (3) | 51 (3) | 0.33 (1) | 34 | |
| 295 | $Sn^0$ | 2.51 (2) | 0.39 (3) | 0.83 (3) | 41 (4) | 0.07 (1) | 56 | 0.5 |
| | $Sn^{II}$ | 3.27 (2) | 1.62 (3) | 0.99 (*) | 59 (3) | 0.12 (3) | 44 | |

Isomer shifts relative to $BaSnO_3$ $\delta$ (mm/s), quadruple splitting $\Delta$ (mm/s), line width at half-maximum $\Gamma$ (mm/s), relative area of the sub-spectra SF (%), Lamb–Mössbauer factor $f$, effective fraction (EF) and refinement quality $\chi^2$. "*" represents fixed values.

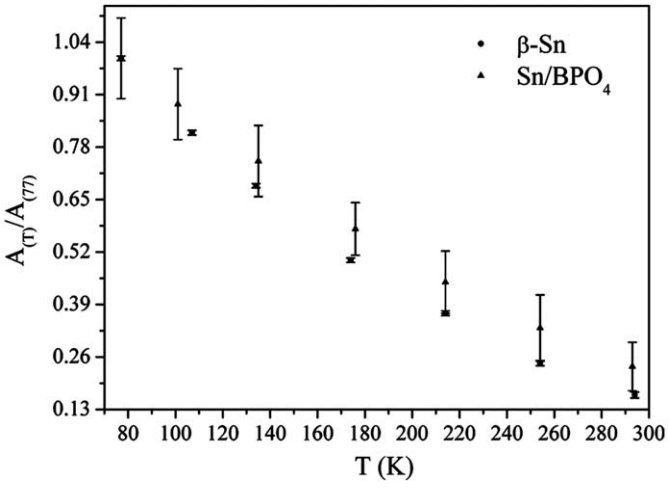


**Fig. 7.** Comparison of the normalized peak areas the commercial β-Sn and the tin present in the $Sn_{0.72}[BPO_4]_{0.28}$ composite.

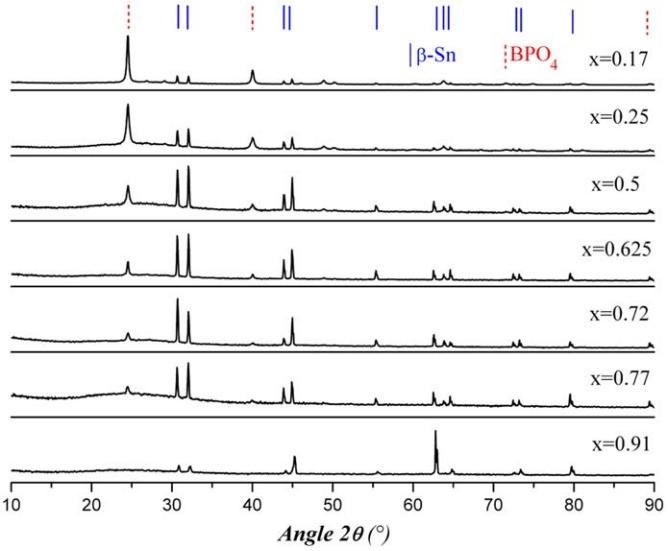


**Fig. 8.** Powder XRD diffraction patterns for the different $Sn_x[BPO_4]_{1-x}$ samples ($\lambda_{CuK\alpha}$=1.5418 Å). Dotted and solid vertical lines denote $BPO_4$ and β-Sn reflections.

the interfacial reduction of $Sn^{II}$ to $Sn^0$ described in our previous work [20].

## 5. Conclusion

The comparative Mössbauer study of amorphous $SnB_{0.6}P_{0.4}O_{2.9}$ and $Sn_{0.72}[BPO_4]_{0.28}$ composite has shown the presence of similar sites in the two materials. The $SnB_{0.6}P_{0.4}O_{2.9}$, obtained by *in-situ* dispersion of SnO into an oxide matrix, exhibits the presence of two $Sn^{II}$ sites with specific Mössbauer parameters of $\delta$=3.02(2) mm $s^{-1}$ and $\Delta$=2.06(3) mm $s^{-1}$ for $Sn^{II}_1$ and $\delta$=3.29(2) mm $s^{-1}$ and $\Delta$=1.70(3) mm $s^{-1}$ for $Sn^{II}_2$. The $Sn_{0.72}[BPO_4]_{0.28}$, obtained by *ex-situ* dispersion of commercial β-Sn into a $BPO_4$ matrix, exhibits a more complex structure involving metallic tin ($\delta$=2.51(2) mm $s^{-1}$, $\Delta$=0.39(3) mm $s^{-1}$) and an oxidized $Sn^{II}$ very similar to $Sn^{II}_2$ in $SnB_{0.6}P_{0.4}O_{2.9}$ ($\delta$=3.27(2) mm $s^{-1}$, $\Delta$=1.62(3) mm $s^{-1}$). CEMS spectra show that this kind of sites is located near the surface of $Sn_{0.72}[BPO_4]_{0.28}$ particles causing metallic tin to be embedded and fixed into its matrix. The calculation of the specific Lamb–Mössbauer factors for the $Sn^0$ and $Sn^{II}$ sites gives a new insight in this interesting anode material.

In the case of $SnB_{0.6}P_{0.4}O_{2.9}$, the Sn formation due to the reaction of the first two lithium ions with $Sn^{II}$–O, leads to the production of quantity of inactive $Li_2O$ resulting in a 60% capacity loss respect to the successive cycles. This mechanism is much more contained in the case of $Sn_{0.72}[BPO_4]_{0.28}$ with a resulting 29% capacity loss after the first cycle in the same experimental conditions. Moreover, this latter composite is lighter than the ATCO, resulting in an higher overall capacity per weight unit. Thanks to the $Sn^{II}$ sites then, the dimensional stability of the composite is prolonged during galvanostatic cycling.

**Table 6**
Hyperfine parameters calculated from $^{119}$Sn Mössbauer spectra at room temperature for all compositions.

| $Sn_x$ | Site Sn | TMS | | | | | CEMS | | | | |
|---|---|---|---|---|---|---|---|---|---|---|---|
| | | $\delta$ | $\Delta$ | $\Gamma$ | SF | EF | $\delta$ | $\Delta$ | $\Gamma$ | SF | EF |
| 0.17 | $Sn^0$ | 2.56 (*) | 0.29 (*) | 0.90 (*) | 5 | 3 | – | – | – | – | |
| | $Sn^{II}$ | 3.27 (1) | 1.64 (1) | 1.05 (1) | 95 | 97 | 3.20 (6) | 1.71 (8) | 0.92 (10) | 100 | |
| 0.25 | $Sn^0$ | 2.56 (*) | 0.29 (*) | 0.90 (*) | 5 | 3 | – | – | – | – | |
| | $Sn^{II}$ | 3.27 (1) | 1.63 (1) | 1.07 (1) | 95 | 97 | 3.27 (4) | 1.73 (5) | 0.97 (1) | 100 | |
| 0.5 | $Sn^0$ | 2.48 (1) | 0.62 (1) | 0.78 (3) | 17 | 27 | 2.56 (*) | 0.29 (*) | 0.90 (*) | 13 | 22 |
| | $Sn^{II}$ | 3.28 (3) | 1.62 (1) | 1.00 (*) | 83 | 73 | 3.31 (2) | 1.82 (1) | 1.27 (5) | 87 | 78 |
| 0.625 | $Sn^0$ | 2.51 (1) | 0.42 (2) | 0.82 (2) | 40 | 55 | 2.56 (*) | 0.29 (*) | 0.90 (*) | 21 | 33 |
| | $Sn^{II}$ | 3.30 (1) | 1.60 (2) | 0.93 (*) | 60 | 45 | 3.22 (2) | 1.63 (1) | 1.06 (1) | 79 | 67 |
| 0.72 | $Sn^0$ | 2.51 (2) | 0.39 (3) | 0.83 (3) | 41 | 56 | 2.56 (*) | 0.29 (*) | 0.90 (*) | 12 | 20 |
| | $Sn^{II}$ | 3.27 (2) | 1.62 (3) | 0.99 (*) | 59 | 44 | 3.29 (2) | 1.65 (3) | 1.01 (5) | 88 | 80 |
| 0.77 | $Sn^0$ | 2.60 (2) | 0.27 (4) | 0.67 (6) | 51.5 | 66 | 2.51 (3) | 0.54 (5) | 0.85 (9) | 29 | 43 |
| | $Sn^{II}$ | 3.16 (3) | 1.81 (4) | 0.91 (*) | 48.5 | 34 | 3.30 (2) | 1.66 (2) | 1.00 (*) | 71 | 57 |
| 0.91 | $Sn^0$ | 2.51 (2) | 0.37 (2) | 0.97 (2) | 74 | 84 | 2.49 (3) | 0.40 (6) | 0.66 (12) | 17 | 24 |
| | $Sn^{II}$ | 3.33 (4) | 1.54 (7) | 0.96 (*) | 26 | 16 | 3.35 (2) | 1.71 (3) | 1.26 (*) | 83 | 73 |

Isomer shifts relative to $BaSnO_3$ $\delta$ (mm/s), quadruple splitting $\Delta$ (mm/s), line width at half-maximum $\Gamma$ (mm/s), relative area of the sub-spectra SF (%) and effective fraction EF (%) calculated for recoilless factor $f$ for each species. "*" represents fixed values.

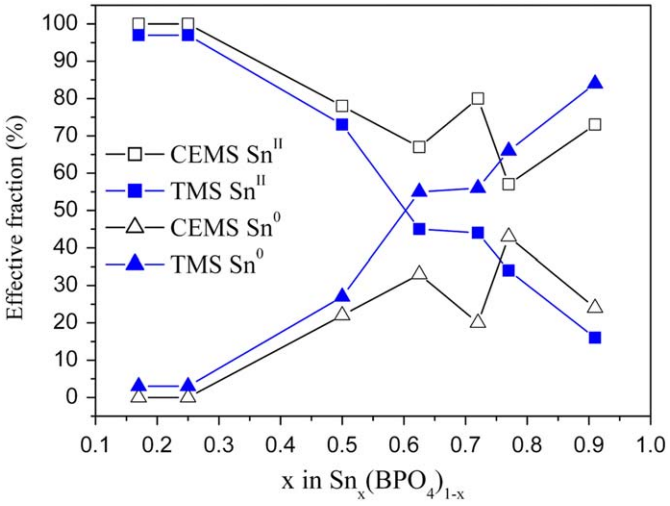


**Fig. 9.** Evolution of the real proportion of $Sn^0$ and $Sn^{II}$ according to the percent of starting β-Sn dispersed in boron phosphate matrix.

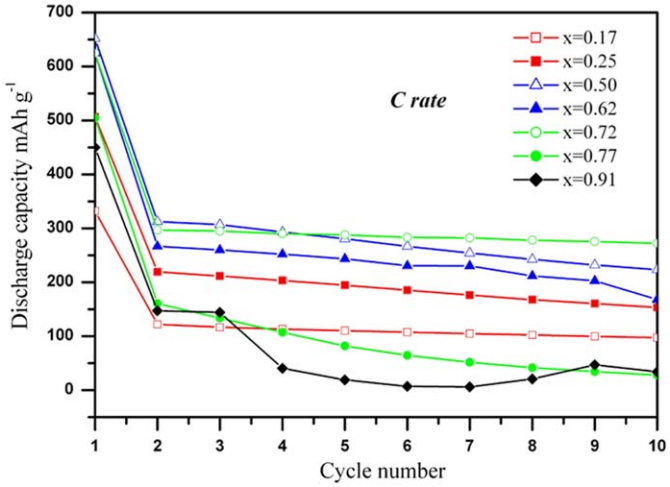


**Fig. 10.** Cycling behaviour of $Sn_x[BPO_4]_{1-x}$ ($0.17 < x < 0.91$) composite electrodes in a Swagelok$^{TM}$ cell at C rate. The specific capacities were calculated taking into account the mass of the inactive boron phosphate matrix. Lines are a guide to the eye.

Among a wide series of stoichiometries, $Sn_{0.72}[BPO_4]_{0.28}$ exhibits interesting performances (reversible capacity of 500 mAh g$^{-1}$ at C/5 rate) as negative electrode material for secondary lithium batteries. Further work is now in progress to understand the organization of the interface between Sn and $BPO_4$ particles and reduce the irreversible capacity observed in the first discharge. The optimization of the active/inactive molar ratio and an improved stability of the interface between the inactive matrix and the active species are, thus, the keys for a new and better performing generation of composite materials for rechargeable lithium ion cells.

## Acknowledgments

This authors express their sincere gratitude to Centre National d'Etudes Spatiales CNES-France (Contract no 60255/00), to CNES-Région Languedoc Roussillon (Contract no 07-011380) to SAFT-France (Contract no 016113) and to the Agence Nationale de la Recherche (Contract no ANR-07-Stock-E-03-02) for financial supports.

## References

[1] J. Yang, M. Winter, J.O. Besenhard, Solid State Ionics 90 (1996) 281.
[2] J.O. Besenhard, J. Yang, M. Winter, J. Power Sources 68 (1997) 87.
[3] A.H. Whitehead, J.M. Elliott, J.R. Owen, J. Power Sources 81–82 (1999) 33.
[4] M. Noh, Y. Kim, M.G. Kim, H. Lee, H. Kim, Y. Kwon, Y. Lee, J. Chao, Chem. Mat. 17 (2005) 3320.
[5] H. Li, J.Y. Zhu, X.J. Huang, L.Q. Chen, J. Mater. Chem. 10 (2000) 693.
[6] K.D. Kepler, J.T. Vaughey, M.M. Thackeray, Electrochem. Solid-State Lett. 2 (1999) 307.
[7] D.G. Kim, H. Kim, H.-J. Sohn, T. Kang, J. Power Sources 104 (2002) 221.
[8] C.M. Ionica-Bousquet, P.-E. Lippens, L. Aldon, J. Olivier-Fourcade, J.-C. Jumas, Chem. Mat. 18 (2006) 6442.
[9] H. Kim, Y.-J. Kim, D.J. Kim, H.-J. Sohn, T. Kang, Solid State Ionics 144 (2001) 41.
[10] D. Larcher, A.S. Prakash, J. Saint, M. Morcrette, J.-M. Tarascon, Chem. Mater. 16 (2004) 5502.
[11] D. Larcher, S. Beattie, M. Morcrette, K. Edström, J.-C. Jumas, J.-M. Tarascon, J. Mater. Chem. 17 (2007) 3759.
[12] H. Fujimoto, A. Minami, Y. Aotsuka, Fuji Photo Film CO., Eur. Patent, (1995) 0 704 921 A1.
[13] Y. Idota, T. Kubota, A. Matsufuji, Y. Maekawa, T. Miyasaka, Science 276 (1997) 1395.
[14] I.A. Courtney, J.R. Dahn, J. Electrochem. Soc. 144 (1997) 2045.
[15] K. Furuya, K. Agawa, Y. Mineo, A. Matsufuji, J. Okuda, T. Erata, J. Phys. Condens. Mater. 13 (2001) 3519.
[16] I.A. Courtney, R.A. Dunlap, J.R. Dahn, Electrochem. Acta 45 (1999) 51.
[17] J. Chouvin, C. Perez-Vicente, J. Olivier-Fourcade, J.-C. Jumas, B. Simon P. Biensan, Solid State Sci. 6 (2004) 39.

[18] J.-C. Jumas, F. Robert, P.-E. Lippens, J. Olivier-Fourcade, P. Willmann, Patent PCT, (2004) WO J.C. 2006/02/17 14012.
[19] A. Aboulaich, M. Mouyane, F. Robert, P.-E. Lippens, J. Olivier-Fourcade, P. Willmann, J.-C. Jumas, J. Power Sources 174 (2007) 1224.
[20] A. Aboulaich, F. Robert, P.-E. Lippens, J. Olivier-Fourcade, P. Willmann, J.-C. Jumas, Hyp. Interact. 167 (2006) 733.
[21] O. Mao, R.A. Dunlap, J.R. Dahn, J. Electrochem. Soc. 146 (1999) 405.
[22] O. Mao, J.R. Dahn, J. Electrochem. Soc. 146 (1999) 414.
[23] J. Chouvin, C. Branci, J. Sarradin, J. Olivier-Fourcade, J.-C. Jumas, B. Simon, P. Biensan, J. Power Sources 81–82 (1999) 277.
[24] W. Kündig, Nucl. Inst. Meth. 75 (1969) 336.
[25] J.I. Corredor, B. León, C. Perez Vicente, J.L. Tirado, J. Phys. Chem. C 112 (2008) 17436.
[26] Z. Edfouf, M.J. Aragón, B. León, C. Perez Vicente, J.L. Tirado, J. Phys. Chem. C 113 (2009) 5316.
[27] F. Robert, P.-E. Lippens, J. Olivier-Fourcade, J.-C. Jumas, F. Gillot, M. Morcrette, J.-M. Tarascon, J. Solid State Chem. 180 (2007) 339.
[28] J. G. Stevens, V. E. Stevens, Mössbauer handbook series: Tin-119, 1990.
[29] R.H. Herber, J. Inorg. Nucl. Chem. 35 (1973) 67.
[30] O. Lindqvit, F. Wengelin, Ark. Kemi. 28 (1967) 179.
[31] J.A. Lee, G.V. Raynor, Proc. Phys. Soc. B 67 (1954) 737.
[32] G.E.R. Schulze, Z. Physik. Chemie B 25 (1934) 215.
[33] R.W.G. Wyckoff, Crystal Structures 3 27.
[34] P.G. Appleyard, J.A. Johnson, C.E. Johnson, M.F. Thomas, D. Holland, A. Sears, J. Phys.: Condens. Matter 9 (1977) 7477.
[35] A. Paul, J.D. Donaldson, M.T. Donoghue, M.J.K. Thomas, Phys. Chem. Glasses 18 (1977) 125.
[36] G.S. Collins, T. Kachanowski, N. Benczer-Koller, Phys. Rev. B 19 (1979) 1369.
[37] C. Feldman, Phys. Rev. 117 (2) (1960) 455.
[38] M. Mouyane, L. Aldon, M. Womes, B. Ducourant, J.-C. Jumas, J. Olivier-Fourcade, J. Power Sources 189 (2009) 818.
[39] J.L. Solis, J. Frantti, V. Lantto, L. Häggström, M. Wikner, Phys. Rev. B 57 (1998) 13491.
[40] M.S. Moreno, R.C. Mercader, Phys. Rev. B 50 (1994) 9875.
[41] C. Hohenemser, Phys. Rev. 139 (1A) (1965) A185.